

**Climatology, seasonality and trends of oceanic coherent  
eddies**

**Josué Martínez-Moreno<sup>1</sup>, Andrew McC. Hogg<sup>1</sup>, and Matthew H. England<sup>2</sup>**

<sup>1</sup>Research School of Earth Science and ARC Center of Excellence for Climate Extremes, Australian National University, Canberra, Australia

<sup>2</sup>Climate Change Research Centre (CCRC), UNSW Australia, Sydney NSW, Australia

**Key Points:**

- Kinetic energy of coherent eddies contain around 50% of the surface ocean kinetic energy budget.
- Seasonal cycle of the number of coherent eddies and coherent eddy amplitude reveal a 3-6 month lag to wind forcing
- Inverse cascade sets up the seasonal lag of the number and amplitude of coherent eddies.
- The coherent eddy amplitude has increase at a rate of 3 cm per decade since 1993.

15 **Abstract**

16 Ocean eddies influence regional and global climate through mixing and transport  
 17 of heat and properties. One of the most recognizable and ubiquitous feature of oceanic  
 18 eddies are vortices with spatial scales of tens to hundreds of kilometers, frequently re-  
 19 ferred as “mesoscale eddies” or “coherent eddies”. Coherent eddies are known to trans-  
 20 port properties across the ocean and to locally affect near-surface wind, cloud proper-  
 21 ties and rainfall patterns. Although coherent eddies are ubiquitous, yet their climatol-  
 22 ogy, seasonality and long-term temporal evolution remains poorly understood. Thus, we  
 23 examine the kinetic energy contained by coherent eddies and we present the annual and  
 24 long-term changes of automatically identified coherent eddies from satellite observations  
 25 from 1993 to 2019. Around 50% of the kinetic energy contained by ocean eddies corre-  
 26 sponds to coherent eddies. Additionally, a strong hemispherical seasonal cycle is observed,  
 27 with a 3–6 months lag between the wind forcing and the response of the coherent eddy  
 28 field. Furthermore, the seasonality of the number of coherent eddies and their amplitude  
 29 reveals that the number of coherent eddies responds faster to the forcing ( $\sim 3$  months),  
 30 than the coherent eddy amplitude (which is lagged by  $\sim 6$  months). Our analysis high-  
 31 lights the relative importance of the coherent eddy field in the ocean kinetic energy bud-  
 32 get, implies a strong response of the eddy number and eddy amplitude to forcing at dif-  
 33 ferent time-scales, and showcases the seasonality, and multidecadal trends of coherent  
 34 eddy properties.

35 **Plain language summary**36 **1 Introduction**

37 Mesoscale ocean variability with spatial scales of tens to hundreds of kilometers is  
 38 comprised of processes such as vortices, waves, and jets (Ferrari & Wunsch, 2009; Fu et  
 39 al., 2010). These mesoscale processes are highly energetic, and they play a crucial role  
 40 in the transport of heat, salt, momentum, and other tracers through the ocean (Wun-  
 41 sch & Ferrari, 2004; Wyrtki et al., 1976; Gill et al., 1974). Possibly, the most recogniz-  
 42 able and abundant process observed from satellites is mesoscale vortices. Although mesoscale  
 43 vortices are commonly referred to in literature as “mesoscale eddies”, this term is also  
 44 often used to describe the total mesoscale ocean variability (the time-varying component  
 45 of the mesoscale flow), thus, here we will refer to mesoscale vortices as *coherent eddies*.

46 Coherent eddies are quasi-circular currents. According to their rotational direction,  
47 the sea surface height anomaly within a coherent eddy can have a negative or positive  
48 sea surface height anomaly (cold-core and warm-core coherent eddies, respectively). This  
49 characteristic sea surface height signature of coherent eddies has been utilized to auto-  
50 matically identify and track coherent eddies from satellite altimetry (Cui et al., 2020;  
51 Martínez-Moreno et al., 2019; Ashkezari et al., 2016; Faghmous et al., 2015; Chelton et  
52 al., 2007). Automated identification algorithms of coherent eddies have shown their ubiq-  
53 uity in the oceans, with a predominant influence at hotspots of eddy activity such as bound-  
54 ary ~~currents~~ extensions and the Antarctic Circumpolar Current. In these regions, Chel-  
55 ton et al. (2011) estimated that coherent eddies contribute around 40–50% of the mesoscale  
56 kinetic energy (Chelton et al., 2011) and thus a significant fraction of the total kinetic  
57 energy (Ferrari & Wunsch, 2009). Although this unique estimate showcases the impor-  
58 tance of the mesoscale coherent eddy field, the energy contained by coherent eddies was  
59 estimated by extracting the geostrophic velocities within the detected coherent eddies,  
60 thus it is possible it may contain energy from other processes. Coherent eddies are not  
61 only abundant and may have a large proportion of the surface kinetic energy budget, but  
62 they are also essential to ocean dynamics as concluded by many previous studies (Pa-  
63 tel et al., 2020; Schubert et al., 2019; Pilo et al., 2015; Frenger et al., 2015, 2013; Beron-  
64 Vera et al., 2013; Siegel et al., 2011; Hogg & Blundell, 2006).

65 There is broad consensus that mesoscale eddy kinetic energy has a pronounced sea-  
66 sonal variability (Uchida et al., 2017; Kang & Curchitser, 2017; Qiu & Chen, 2004; Qiu,  
67 1999). Several hypotheses have been proposed to explain this seasonality including: sea-  
68 sonal variations of atmospheric forcing (Sasaki et al., 2014), seasonality of the mixed layer  
69 depth (Qiu et al., 2014; Callies et al., 2015), seasonality of the intensity of barotropic in-  
70 stability (Qiu & Chen, 2004), the variability of the baroclinic instability due to the sea-  
71 sonality of the vertical shear (Qiu, 1999), and a seasonal lag of the inverse energy cas-  
72 cade (i.e. energy is transported between scales, from small to large; Arbic et al., 2013)  
73 in combination with the presence of a front in the mixed layer, which can lead to a sea-  
74 sonal cycle of the baroclinic instability (Qiu et al., 2014). On one hand, processes such  
75 as barotropic and baroclinic instabilities control the seasonality of coherent eddies in the  
76 ocean. On the other hand, recent studies using observations and eddy-permitting climate  
77 models suggest several long-term adjustments of the global ocean capable of long-term  
78 changes in the coherent eddy field. Such readjustments include a multidecadal increase

in the ocean stratification resulted from temperature and salinity changes (Li et al., 2020), a horizontal readjustment of the sea surface temperature gradients (Ruela et al., 2020; Bouali et al., 2017; Cane et al., 1997), and an intensification of the kinetic energy, eddy kinetic energy, and mesoscale eddy kinetic energy over the last 3 decades as a consequence of an increase in wind forcing (Hu et al., 2020; Wunsch, 2020; Martínez-Moreno et al., 2021). All these seasonal factors and long-term readjustments directly influence the annual and decadal response of the coherent eddy field, however, the seasonality of the coherent component of the eddy kinetic energy, as well as the seasonal cycle and trends of the coherent eddy statistics remain unknown.

Here we present a new global climatology of the coherent eddy kinetic energy by reconstructing the coherent eddy signature from satellite observations. Our study documents the seasonal cycle of the coherent eddy kinetic energy, and seasonal cycle and long-term trends of the coherent eddy properties over the satellite record. Moreover, we conduct more detail analysis in regions where coherent eddies dominate the eddy kinetic energy field. This paper is structured as follows: the data sources and methodology are described in section 2. Then, we present the climatology, energy ratios, and global seasonality of the coherent eddy kinetic energy in section 3. Section 4 presents the global climatology and seasonality of coherent eddy properties, followed by long-term changes of the coherent eddy properties (section 5). Then we focus our attention on the seasonal cycle and coherent eddy properties in regions dominated by coherent eddies (section 6). Finally, section 7 summarizes the main results and discusses the implications of this study.

## 2 Methods

We use daily sea surface height (SSH) data made available by the Copernicus Marine Environment Monitoring Service in near real time (CMEMS, 2017). This gridded product contains the sea surface height and geostrophic velocities with daily  $0.25^{\circ}$  resolution from January 1993 to 2019. The daily geostrophic velocities allowed us to compute the kinetic energy (KE) and eddy kinetic energy (EKE) over the satellite record. The main source of EKE is the time-varying wind (Ferrari & Wunsch, 2009), thus we computed the seasonal cycle of the wind magnitude from the JRA55 reanalysis (Japan Meteorological Agency, Japan, 2013) using wind velocities at 10m above the ocean's surface.

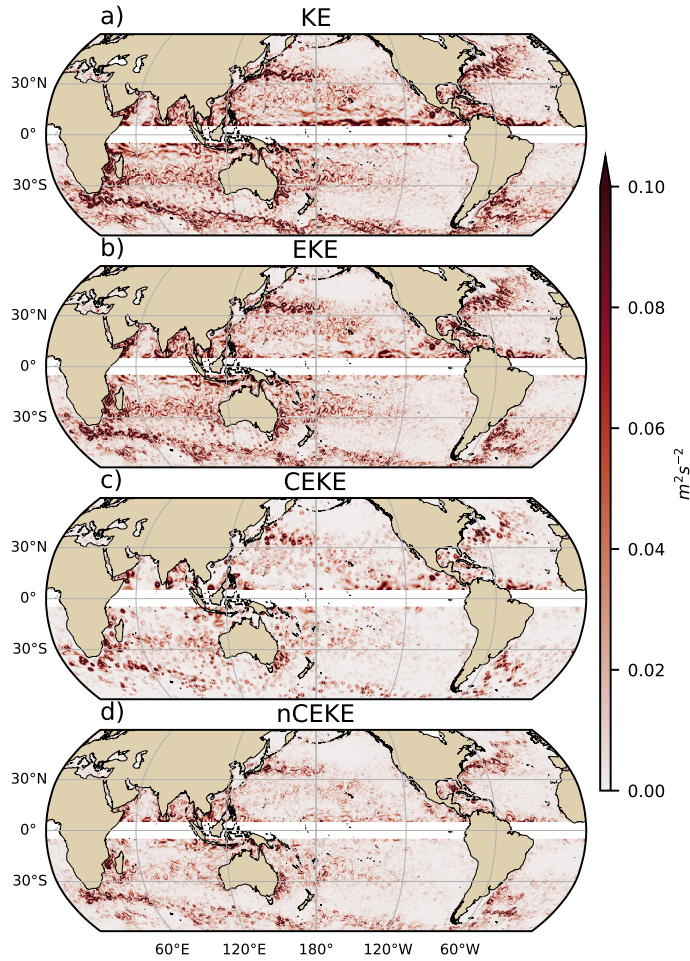
Over the same record, coherent eddy statistics from Martínez-Moreno et al. (2019), hereafter M-M, are analyzed and compared to those released by Chelton & Schlax (2013), both datasets are gridded in a  $1^\circ$  resolution. Although both datasets are produced via automated eddy identification algorithms using closed contours of SSH, these datasets have important differences in the criteria they use to identify and record coherent eddies statistics. The major differences include; (i) M-M's algorithm requires an adjustment between a 2D Gaussian and the SSH anomaly (SSHa) surface within the identify closed contour, while Chelton's only uses the outer-most closed contour of SSH; (ii) M-M's dataset reports the maximum SSHa within the identified coherent eddy, while Chelton's algorithm reports the maximum SSH value minus the discrete level in which the coherent eddy was identified; M-M's dataset includes all detected coherent eddies, while Chelton's dataset excludes (iii) coherent eddies with lifetimes shorter than four weeks and (iv) coherent eddy amplitudes smaller than 1cm. Moreover, M-M's algorithm allows the reconstruction of the coherent eddy field under the assumption that coherent eddies have a 2D Gaussian imprint in the sea surface height. This Gaussian reconstruction of the coherent eddy field then allow us to estimate the coherent geostrophic eddy velocities and thus the kinetic energy contained only by coherent eddies.

## 2.1 Kinetic Energy decomposition

Kinetic energy is commonly divided into the mean and time-varying components through a Reynolds decomposition. At a given time, the surface velocity field  $\mathbf{u} = (u, v)$  is split into the time mean ( $\bar{\mathbf{u}}$ ) and time varying components ( $\mathbf{u}'$ ). Moreover, M-M proposed to further decompose the eddy kinetic energy into the energy contained by coherent features ( $\mathbf{u}'_e$ ) and non-coherent features ( $\mathbf{u}'_n$ ). Therefore the KE equation can be written as:

$$\text{KE} = \underbrace{\bar{u}^2 + \bar{v}^2}_{\text{MKE}} + \underbrace{u'^2_e + v'^2_e + u'^2_n + v'^2_n}_{\text{CEKE}} + \underbrace{\mathcal{O}_c^2}_{\text{nCEKE}} + \mathcal{O}^2 \quad (1)$$

Due to the properties of this decomposition, the second order term  $\mathcal{O}^2$  is zero when averaged over the same period as  $\bar{\mathbf{u}}$ . However,  $\mathcal{O}_c^2$  is not necessarily negligible, unless it is averaged over time and space. More information about the decomposition of the field into coherent features and non-coherent features is explained by Martínez-Moreno et al.



143 **Figure 1.** Snapshot of surface kinetic energy ( $\overline{KE}$ ), surface eddy kinetic energy ( $\overline{EKE}$ ),  
 144 surface coherent eddy kinetic energy ( $\overline{CEKE}$ ), and surface non-coherent eddy kinetic energy  
 145 ( $\overline{nCEKE}$ ) for the 1st of January 2017.

138 (2019). A global snapshot of each component of kinetic energy decomposition is shown  
 139 in Figure 1, where the KE and EKE are comprised of rings and filaments. As expected,  
 140 the decomposition of EKE into CEKE and nCEKE components exhibit only ring-like  
 141 signatures expected of coherent eddies, while the non-coherent component shows filaments  
 142 and some miss-identified coherent eddies.

## 146 2.2 Eddy statistics

147 The eddy statistics used in this study include (i) the eddy count ( $cEddy_n$ ) defined  
 148 as the number of eddies per grid cell, (ii) the eddy diameter defined as the diameter of

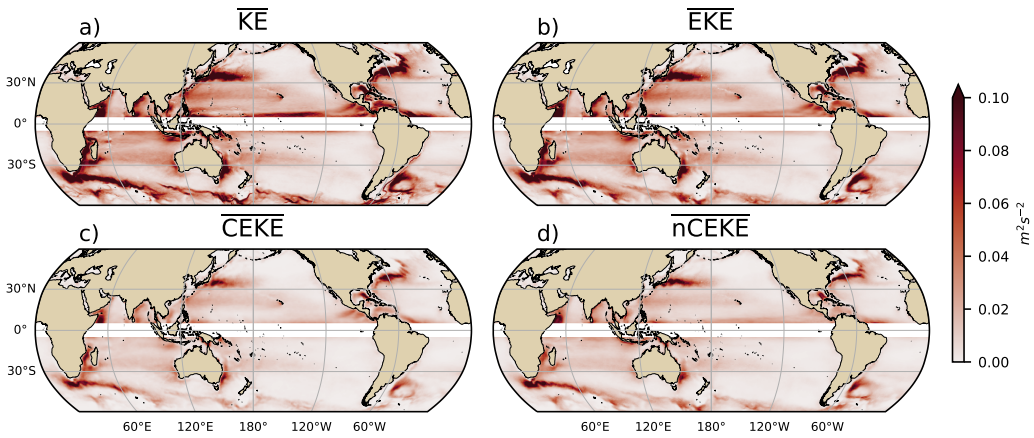
a circle with equal area as the closed contour of the identified eddy, and (iii) the mean eddy amplitude defined as the mean amplitude of the coherent eddies within the cell ( $cEddy_{amp}$ ). The latter metric can be separated into positive ( $cEddy_{amp}^+$ ) and negative ( $cEddy_{amp}^-$ ) coherent eddy amplitudes, defined as the mean amplitude of warm core and cold core coherent eddies, respectively, within the cell. The absolute eddy amplitude ( $|cEddy_{amp}|$ ) is then defined as:

$$|cEddy_{amp}| = \frac{1}{2} (cEddy_{amp}^+ - cEddy_{amp}^-) \quad (2)$$

Note that the  $cEddy_{amp}^+$  and  $cEddy_{amp}^-$  are sign definite, thus the difference will always be positive, mean  $cEddy_{amp}$  can be negative or positive noting the dominant polarity of coherent eddies in the region. We analyze the climatology, seasonal cycles and trends of the eddy statistics between 1993 and 2019. We exclude the equatorial region ( $10^\circ\text{S}$  -  $10^\circ\text{N}$ ) and poleward of  $60^\circ$ . Note that the climatology of  $cEddy_n$  is computed by adding all the identified eddies over the record, while all other climatological statistics are computed as the time-average over the record. Seasonal climatologies are calculated for the monthly average of each coherent eddy statistic, while hemispherical time-series are filtered with a running average of 90 days. Trends of  $cEddy_n$  and  $|cEddy_{amp}|$  are calculated by coarsening the dataset to a  $5^\circ$  grid, and then linear trends are computed for each grid point, the statistical significance is assessed by a modified Mann-Kendall test (Yue & Wang, 2004). Time averages are denoted by  $\overline{\phantom{x}}$ , while time and area averages are shown by  $\langle \phantom{x} \rangle$ .

### 3 Global Coherent Eddy Energetics

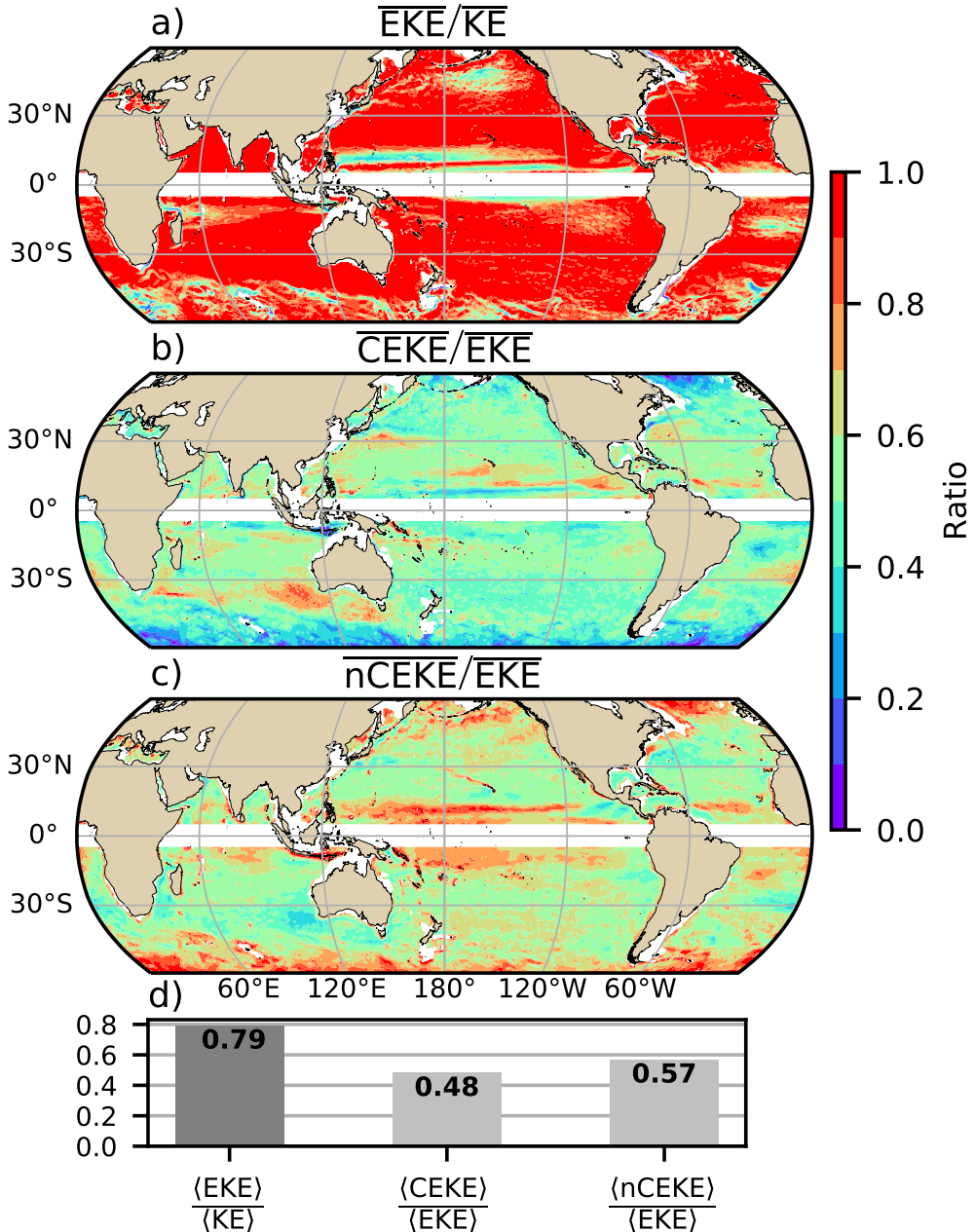
The ~~climatology of the~~ kinetic energy decomposition estimated from sea surface height measured by satellite altimeters is shown in Figure 2. These maps show that many regions of the global ocean are highly energetic in mean KE ( $\overline{KE}$ ), mean EKE ( $\overline{EKE}$ ), mean coherent eddy kinetic energy ( $\overline{CEKE}$ ) and mean non-coherent eddy kinetic energy ( $\overline{nCEKE}$ ). The spatial pattern highlights well known regions of the ocean ~~where mesoscale processes are abundant, such as the case of western boundary currents, as the western boundary extensions and~~ the Antarctic Circumpolar Current ~~and regions within the ocean gyres.~~ Remarkably, the spatial distribution of the energy contained by the reconstructed mesoscale coherent eddies and non-coherent components are similar (Figures 2c,d). ~~This can be thought as regions where mesoscale activity is intense, however,~~ However, there are some regions where coherent eddies dominate over non-coherent and vice-versa. Overall, this



183 **Figure 2.** Climatology of Mean surface kinetic energy ( $\overline{KE}$ ), surface eddy kinetic energy  
 184 ( $EKE$ ), surface coherent eddy kinetic energy ( $\overline{CEKE}$ ), and surface non-coherent eddy kinetic  
 185 energy ( $\overline{nCEKE}$ ) between 1993-2018.

180 decomposition suggest that boundary ~~currents~~current extensions and other energetic  
 181 regions, in particular, eddy-rich regions in the ocean contain both coherent and non-  
 182 coherent components of the kinetic energy.

185 Eddy kinetic energy is known to be more than an order of magnitude greater than  
 186 MKE (Gill et al., 1974),~~this~~; this result is clearly shown in Figure 3a, where ~~the ratio~~  
 187 ~~of~~  $EKE$  is responsible ~~of~~ for almost all the  $\overline{KE}$  across the ocean, except for regions with  
 188 persistent currents over time. Such regions are located in the mean boundary ~~current~~  
 189 extension locations, the equatorial ~~Pacific~~Pacific currents and regions in the Antarctic  
 190 Circumpolar ~~current~~Current, where the  $EKE$  explains around 40% of the  $\overline{KE}$ . ~~As estimated~~  
 191 ~~by~~ In a previous study~~by Chelton et al. (2011)~~, Chelton et al. (2011) estimated that  
 192 the EKE within coherent eddies with lifetimes greater than 4 weeks contain between 40  
 193 to 60 percent of the  $\overline{EKE}$ . Our ~~result from reconstructing method to reconstruct~~ the co-  
 194 herent eddy signature (Figure 3b) further corroborates that the coherent component ( $\overline{CEKE}$ )  
 195 has ~~around~~ ~48% of the  $\overline{KE}$  (Figure 3d). Furthermore, global area averages of the ra-  
 196 tios show  $EKE$  explains ~~approximately~~ ~78% of the ocean  $\overline{KE}$  field, while non coherent  
 197 eddy features contain ~~~~~57% of the  $\overline{EKE}$ . Note the globally averaged coherent  
 198 and non coherent components do not add to 100% as the cross terms ( $O_c^2$ ) are ~~different~~  
 199 ~~to zero~~non-zero, as regions with ~~negligible~~weak EKE are double counted in the  $\overline{CEKE}$   
 200 and  $\overline{nCEKE}$  ratios, and coherent eddy reconstruction errors. The spatial pattern reveals  
 201



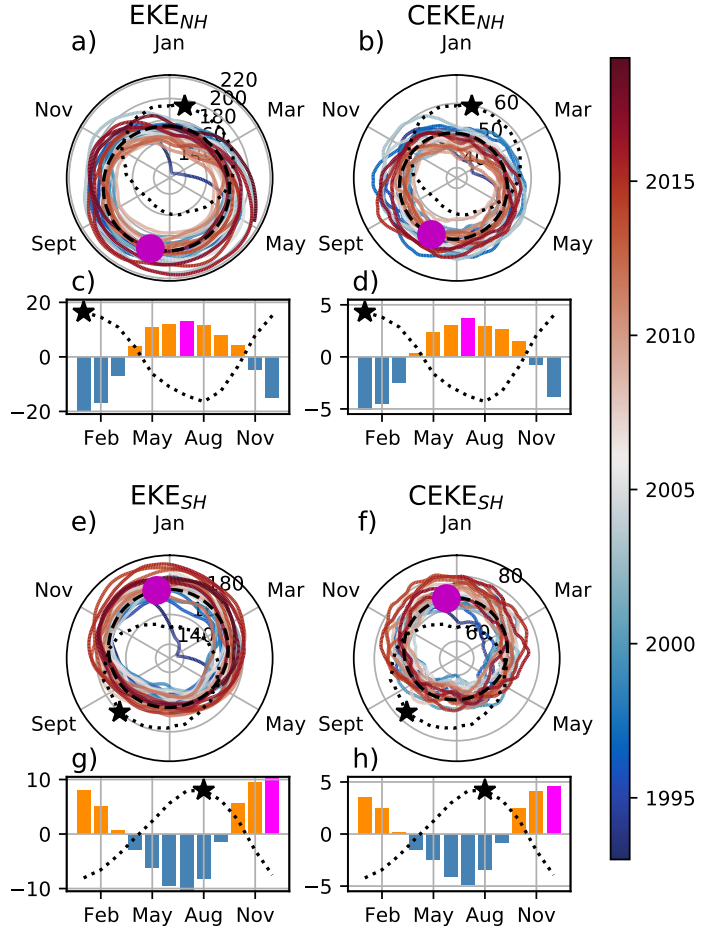
186 **Figure 3.** Ratios of the kinetic energy components. a) Map of the proportion of mean eddy  
 187 kinetic energy ( $EKE/\overline{KE}$ ) versus mean kinetic energy ( $\overline{KE}$ ); b) Map of the percentage of mean  
 188 coherent eddy kinetic energy ( $CEKE/\overline{EKE}$ ) versus mean eddy kinetic energy ( $\overline{EKE}$ ); c) Map of the  
 189 percentage of mean non-coherent eddy kinetic energy ( $nCEKE/\overline{EKE}$ ) versus mean eddy kinetic energy  
 190 ( $\overline{EKE}$ ); d) Global time and area averaged (represented by ⟨ ⟩) percentage of mean eddy kinetic  
 191 energy ( $\langle \overline{EKE} \rangle$ ) versus the global mean kinetic energy ( $\langle \overline{KE} \rangle$ ), area averaged percentage of mean  
 192 coherent eddy kinetic energy ( $\langle CEKE \rangle$ ) and mean non coherent eddy kinetic energy ( $\langle nCEKE \rangle$ )  
 193 versus global mean eddy kinetic energy ( $\langle \overline{EKE} \rangle$ ). Regions where the depth of the ocean is shallower  
 194 than 1000m are removed from the ratio estimation.

a dominance of the CEKE equatorward from the boundary ~~currents~~extensions and areas with large coherent eddy contributions of around 80% of the region's eddy kinetic energy can be found south of Australia, the Tehuantepec Gulf, and the ~~South~~tropical Atlantic. An evident signal is an reduction of the energy contained by coherent eddies at high latitudes and an increase in the energy explained by non-coherent eddies,~~this~~; this signal could be a consequence of the incapability of the  $0.25^{\circ}$  satellite resolution ( $\sim 13$  km at  $60^{\circ}$ ) to resolve coherent eddies with scales smaller than  $\sim 10$  km (first baroclinic Rossby radius at  $60^{\circ}$ ; Chelton et al. 1998).

### 219 3.1 Seasonality

220 Figure 4 shows the seasonal cycle of the EKE and CEKE for the ~~northern hemisphere~~  
 221 Northern Hemisphere (NH;  $10^{\circ}\text{N}$  -  $60^{\circ}\text{N}$ ) and Southern Hemisphere (SH;  $60^{\circ}\text{S}$  -  $10^{\circ}\text{S}$ ).  
 222 In both hemispheres, the EKE and CEKE peak during ~~the hemispherical~~ summer. In  
 223 the ~~northern hemisphere~~Northern Hemisphere, the largest EKE and CEKE occurs  $\sim 6$   
 224 months after the maximum winds (Figure 4c and d), while the Southern ~~ocean~~Ocean  
 225 seems to respond within  $\sim 4$  months (Figure 4g, and h). This seasonal lag and maximum  
 226 is consistent with a time-lag of the inverse cascade (Sasaki et al., 2014; Qiu et al., 2014)  
 227 where winter has the highest energy at the smallest scales (~~non-solvable~~non-resolvable  
 228 with satellite observations), spring and autumn have the highest and lowest energy in  
 229 scales of 50-100 km, and summertime has the highest energy at the largest scales ( $> 100$   
 230 km; Uchida et al. 2017),~~thus~~. Thus, the maximum of EKE and CEKE located during  
 231 summertime suggest that the seasonality of eddies and coherent eddies could be dom-  
 232 inated by scales larger than 100 km.

233 The cyclic plots in Figure 4 ~~shows~~show the temporal evolution of EKE and CEKE.  
 234 Note that high frequency variability can be observed in the CEKE field with temporal  
 235 scales of a few months, this could be attributed local dynamics averaged over the hemi-  
 236 sphere, as well as errors within the coherent eddy reconstruction. Additionally, cyclic  
 237 plots highlight long-term temporal changes over the record; (i) ~~northern hemisphere~~Northern  
 238 Hemisphere winters show a decrease in the CEKE field and (ii) the Southern ~~hemisphere~~  
 239 Hemisphere show concentric growth over time in EKE and CEKE, which support the  
 240 increasing trends in the Southern Ocean observed by Hogg et al. (2015), Martínez-Moreno  
 241 et al. (2019), and Martínez-Moreno et al. (2021).



242 **Figure 4.** Hemispherical seasonality of eddy kinetic energy (EKE), coher-  
 243 ent eddy kinetic energy (CEKE). Panels a and b show the northern hemisphere seasonal  
 244 cycle time-series of the Northern Hemisphere, while panels e and f correspond to the southern  
 245 hemisphere. Panels c and d show the seasonal cycle of the EKE and CEKE  
 246 in the Northern Hemisphere, and panels g and h show the Southern Hemisphere. Dashed lines  
 247 correspond to the seasonal cycle of the fields and dotted lines show the seasonal cycle of the  
 248 wind magnitude smoothed over 120 days (moving average). The green/black and magenta stars  
 249 markers (circle and bar) show the maximum of the seasonal cycle for the kinetic energy com-  
 250 ponents and the wind magnitude, respectively. The In cyclic plots, line colors shows the  
 251 year.

## 252 4 Global Coherent Eddy Statistics

253 Automated ~~algorithms allows coherent eddy identification algorithms allow us~~ to  
 254 estimate the contribution and temporal changes of eddy properties, in particular, their  
 255 abundance ~~as~~<sup>(the number of eddies)</sup> and their intensity ~~, namely~~<sup>(both)</sup> their amplitude  
 256 and diameter). Figure 5 shows gridded climatologies of the number of eddies and the eddy  
 257 amplitude. We ~~eompare contrast~~ M-M eddy count ~~against with~~ Chelton et al. (2007) (Fig-  
 258 ure 5a-b). Although the number of the identified eddies is larger in M-M, possibly due  
 259 to the lifespan filter implemented by Chelton, both datasets reveal consistent spatial pat-  
 260 terns. For example, both datasets show high abundance of eddies in the East North Pa-  
 261 cific, East North Atlantic, as well as the East South Pacific, East South Atlantic and East  
 262 Indian Ocean, and small number counts of eddies in the tropics and in high latitudes ( $\sim 60^\circ$ ).  
 263 An interesting pattern also emerges in both eddy count datasets, where clusters with larger  
 264 eddy counts are favored across the ocean, ~~in addition, coherent eddy propagation patterns~~  
 265 ~~can be observed in boundary currents~~. In addition, to preferential coherent eddy paths  
 266 ~~observable in boundary extensions~~ and regions in the Southern Ocean. These clusters  
 267 and paths of coherent eddies could be associated with topographic features, however ~~it~~  
 268 ~~remains puzzling the consistency of~~ they remain a puzzling consistency between the eddy  
 269 count pattern ~~using these two eddy identification methods~~.

275 Regions with large counts of eddies have in general small absolute amplitudes (Fig-  
 276 ure 5 c), ocean gyre interiors follow with a larger absolute amplitude and finally regions  
 277 such as the boundary ~~currents extensions~~ and Antarctic Circumpolar Current have the  
 278 largest coherent eddy absolute amplitudes as shown by Chelton et al. (2011). Eddy am-  
 279 plitude highlights regions dominated by a given coherent eddy polarity, for example, bound-  
 280 ary ~~currents extensions~~ have a preferred sign (Figure 5 d); positive amplitude polewards  
 281 of the boundary ~~current extension~~ mean location, and negative amplitude equatorwards.  
 282 This sign preference is consistent with the way coherent eddies are shed from boundary  
 283 ~~currents extensions~~ (Kang & Curchitser, 2013; Chelton et al., 2011, 2007). These global  
 284 statistics reveal the absolute coherent eddy amplitude is a proxy of the CEKE with sim-  
 285 ilar spatial patterns (Figure 2 & Figure 5 c) and showcases that regions where ~~CEKE~~  
 286 has a large proportion of EKE (Figure 3), the absolute coherent eddy amplitude is also  
 287 ~~important~~<sup>large</sup>.

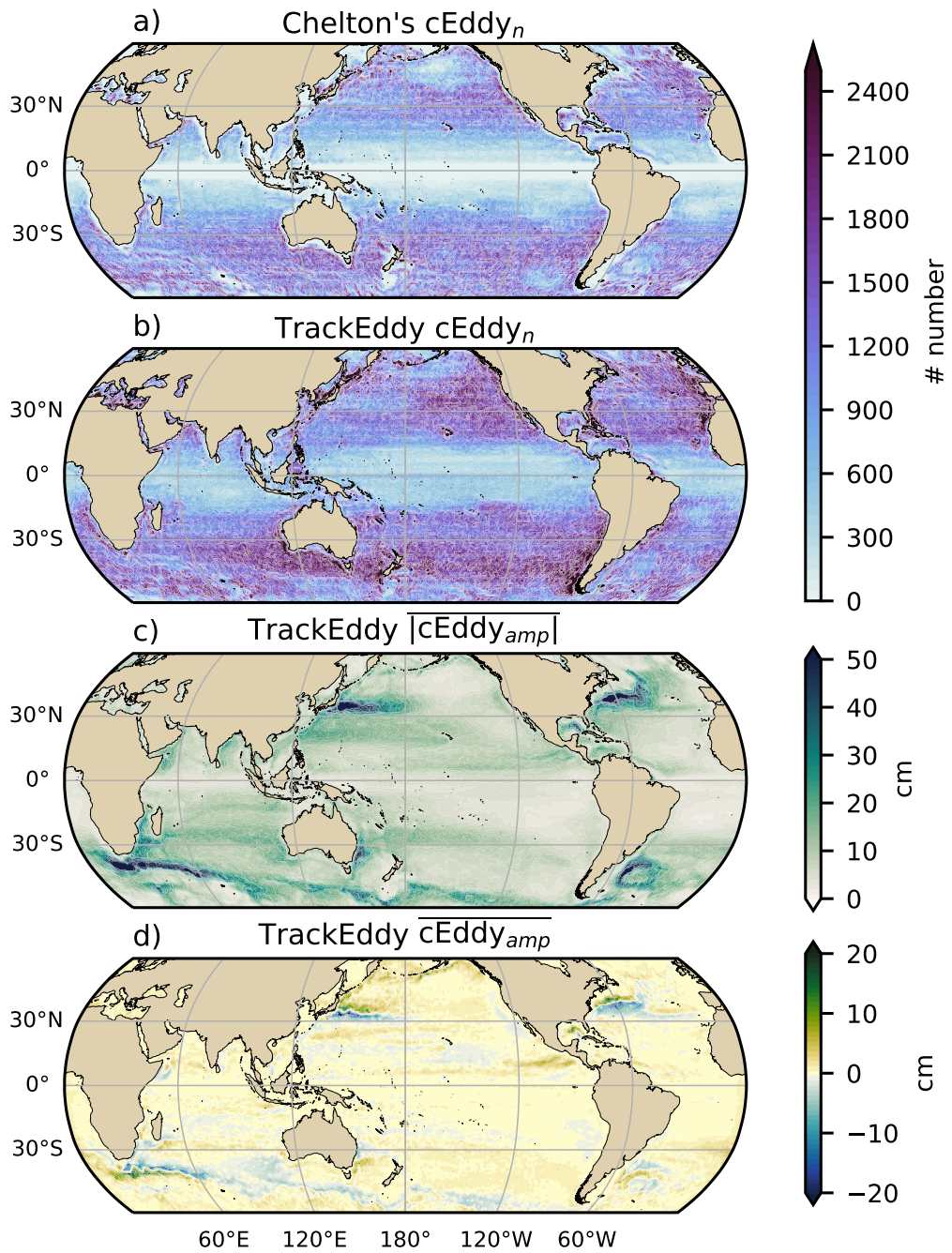


**Figure 5.** Climatology of the Averaged coherent eddy statistics. a) Climatology of the number of coherent eddies ( $cEddy_n$ ) identified by Chelton et al. (2007); b) Climatology of the number of coherent eddies ( $cEddy_n$ ) identified by Martínez-Moreno et al. (2019); c) Climatology of the mean absolute coherent eddy amplitude ( $cEddy_{amp}$ ). d) Climatology of the mean coherent eddy amplitude ( $cEddy_{amp}$ ).

288        **4.1 Seasonality**

To further understand the seasonal cycle of CEKE, we compute ~~hemispherical seasonality of the climatology of~~ coherent eddy properties ~~in each hemisphere~~ (Figure 6). The seasonality of the number of eddies in the Northern Hemisphere peaks on April (Figure 6 a, c), while the Southern Hemisphere maximum number of eddies occurs during October (Figure 6 e, g). Meanwhile, the seasonality of the absolute eddy amplitude peaks in August and January for the Northern and Southern Hemispheres respectively (Figure 6 b, d, f, and h). As expected, the seasonality of the absolute eddy amplitude or intensity of the coherent eddies, is consistent with the seasonal cycle of CEKE. Furthermore, a distinct lag of  $\sim$ 3 months is observed between the winds and eddy count, while the eddy amplitude maximum occurs  $\sim$ 6 months after the seasonal maxima in winds. This lag suggest the eddy number increases earlier in the year and through eddy-eddy interactions (merging of coherent eddies) the amplitude of the coherent eddy increases. This ~~result~~ can be further explored by looking at the ~~seasonal evolution of the~~ eddy diameter. Note that 90% of identified ~~coherent~~ eddies have diameters between 50 to 220 km (Figure 7 a), ~~but more importantly, we observe in the Northern Hemisphere. We divided eddies into~~ large-scale coherent eddies (diameter  $>$  120 km) ~~maximum diameter occur during September, while and~~ small-scale coherent eddies (diameter  $<$  120 km) ~~seasonal peak is during May; Figure 7a). In the Northern Hemisphere, small eddies have a seasonal peak in XXX diameter during May, while large eddies have the greatest diameter in September~~ (Figure 7 b). Meanwhile, in the Southern Hemisphere, the ~~large-seale coherent eddies occurs in February, while the small-seale~~ small-scale coherent eddies have the maximum diameter in December, while large-scale coherent eddies peak in ~~December~~ February (Figure 7 c). This result ~~is consistent with baroclinic instabilities generating many suggests that wind driven baroclinic instabilities generate~~ small coherent eddies early ~~in the season,~~ which then ~~are capable to merge and grow to become larger and in diameter and amplitude,~~ and thus, more energetic. This process ~~can be thought analogous to is associated with~~ the inverse energy cascade, ~~thus and suggest that~~ this mechanism not only drives the EKE seasonality, but also may be responsible of the seasonal cycle of coherent eddies.

317        Long-term changes can be observed in Figure 6a,b, e, and f where growing-shrinking  
 318        concentric circles over time denote an increase-decrease trend of the field. This ~~trend~~ is  
 319        particularly evident in the Southern Hemisphere, where the number of eddies has decreased,  
 320        the eddy amplitude has increased. This result is consistent with the observed trends in

321 EKE and mesoscale EKE in the Southern Ocean (Hogg et al., 2015; Martínez-Moreno et al., 2021)  
 322 Furthermore, by analogy we extend the argument that a long-term decrease in the number  
 323 of coherent eddies and increase in coherent eddy amplitude could be a consequence of  
 324 a long-term increase in the energy cascade, where interactions between eddies may become  
 325 more frequent and result in stronger coherent eddies. This hypothesis may also occur  
 326 in conjunction with other processes, such as baroclinic and barotropic instabilities generating  
 327 stronger eddies. (Hogg et al., 2015; Martínez-Moreno et al., 2019).

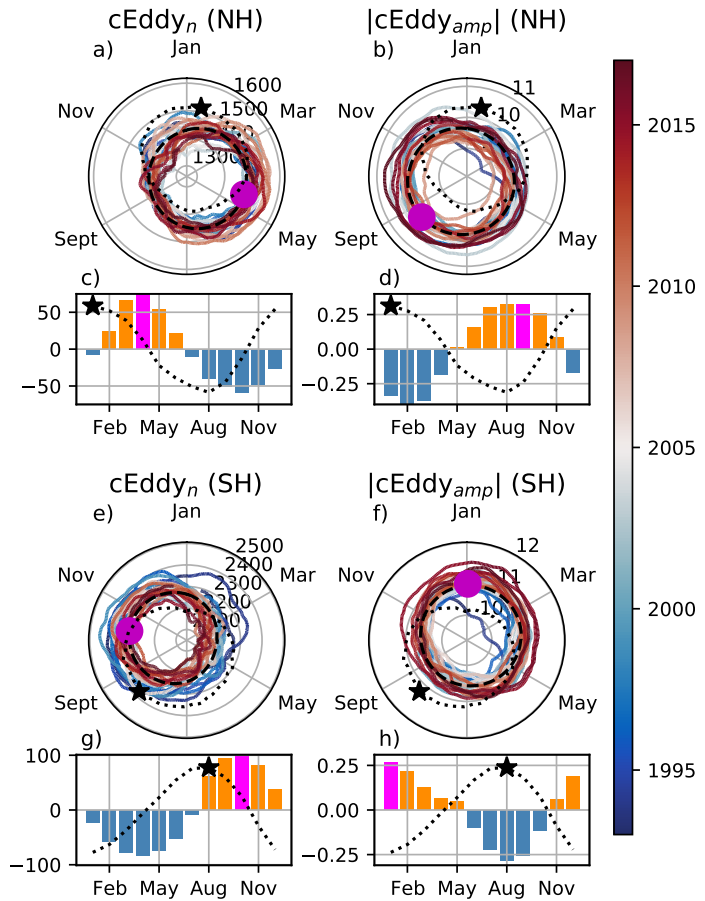
343 The coherent eddy amplitude from positive coherent eddies and negative coherent  
 344 eddies show similar seasonal cycles to the absolute eddy amplitude (Figure 8). However,  
 345 by separating the polarity contribution, it's observed that the amplitude of negative co-  
 346 herent eddies in the Northern Hemisphere has decreased (Figure 8b). In the Southern  
 347 Ocean, the increase in absolute eddy amplitude is further corroborated as both coher-  
 348 ent eddy polarities show an increase since the early 90s (Figure 8e,f).

## 359 5 Trends

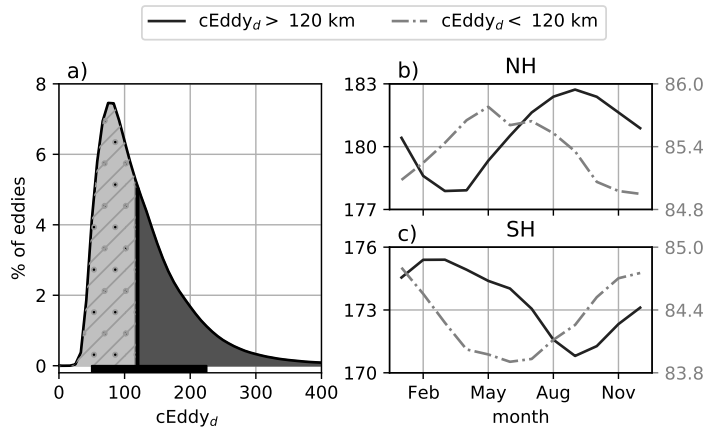
360 It is expected from the results presented in Figures 4, 6, and 8 suggest a long-  
 361 term readjustment of the coherent eddy field. The long-term trends of the number of co-  
 362 herent eddies, absolute coherent eddy amplitude, and coherent eddy amplitude polar-  
 363 ities are explored in Figure 9. Chelton's and M-M datasets show consistent spatial pat-  
 364 terns in the trends and significance of the number of coherent eddies and the absolute  
 365 coherent eddy amplitude. Several regions in the ocean, such as the Southern Ocean, North  
 366 Atlantic and North Pacific, show a decrease in the number of eddies, meanwhile those  
 367 same regions. Those same regions also have a clear increase in the absolute coherent eddy  
 368 amplitude. This collocation of decrease in number and increase in eddy amplitude provides  
 369 more evidence of a possible intensification of the coherent eddy field through eddy-eddy  
 370 interactions. These trends are similar to those observed in mesoscale eddy kinetic en-  
 371 ergy (Martínez-Moreno et al., 2021) and provide additional evidence of a readjustment  
 372 of the mesoscale eddy field over the last 3 decades.

373 Although the observed trends in several regions in the ocean are experiencing  
 374

375 The observed trends of  $|cEddy_{amp}|$  ( $\sim 3\text{cm}$ ) in several oceanic regions have the same  
 376 scale as sea level rise ( $\sim 3\text{cm per decade}$ ) by analyzing the positive and negative coher-



328 **Figure 6.** Hemispherical seasonality of the coherent eddy statistics; a,e) seasonal cycle of the  
 329 number of coherent eddies ( $c\text{Eddy}_n$ ); b,f) seasonal cycle of the mean coherent eddy amplitude  
 330 ( $|c\text{Eddy}_{amp}|$ ); c,g) seasonal cycle of the warm core coherent eddies amplitude (positive  $c\text{Eddy}_{amp}$ );  
 331 d,h) seasonal cycle of the cold core coherent eddies amplitude (negative  $c\text{Eddy}_{amp}$ ). Panels a,b  
 332 and c show the [northern hemisphere](#) [Northern Hemisphere](#) seasonal cycle, while panels d,e, and f  
 333 correspond to the [southern hemisphere](#) [Southern Hemisphere](#). Dashed lines correspond to the sea-  
 334 sonal cycle of the fields and dotted lines show the seasonal cycle of the wind magnitude smoothed  
 over 120 days (moving average). The green and magenta stars show the maximum of the seasonal  
 335 cycle for each field and the wind magnitude, respectively. The line colors show the year.  
 336



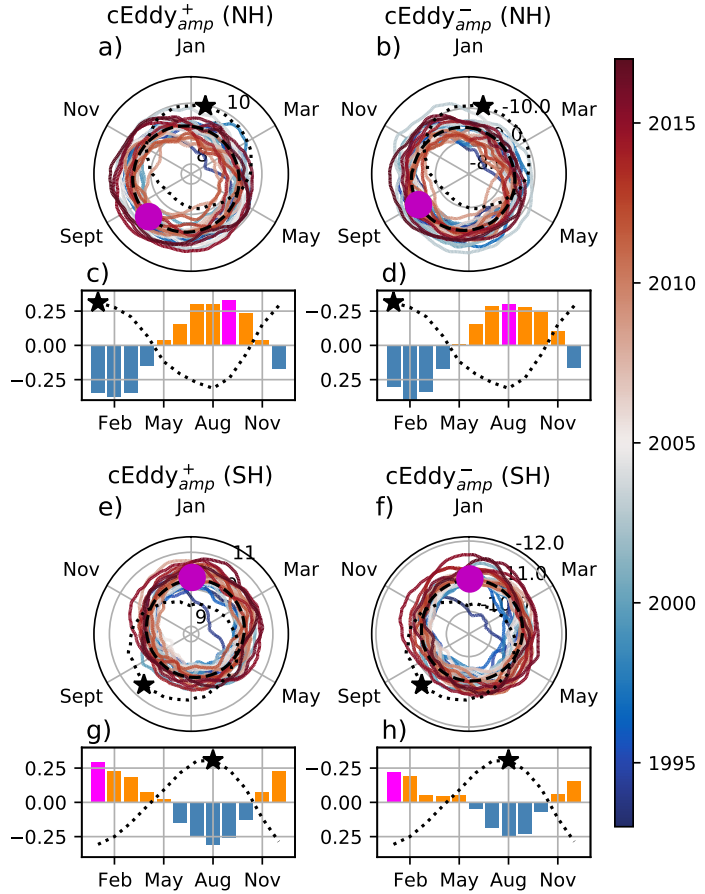
337 **Figure 7.** Distribution of the identified eddy diameter ( $cEddy_d$ ; km) and hemispherical  
 338 seasonality of the coherent eddy diameter. a) Distribution in percentage of identified eddy am-  
 339 plitude, solid bar below distribution represents 90% of the identified eddies. Seasonal cycle of  
 340 the eddy diameter for the b) Northern Hemisphere and c) Southern Hemisphere. Dark solid line  
 341 and area corresponds to coherent eddies with diameters larger than 120 km, while light gray  
 342 dash-dotted line and area shows coherent eddies with diameters smaller than 120 km.

377 ent eddy amplitude we can discard the observed trends correspond to an increase in sea  
 378 level. In fact, each coherent eddy polarity has intensified in the Southern Ocean and North  
 379 East Pacific and Atlantic. In other words, the absolute amplitude of each polarity has  
 380 increased over time, thus this strengthening is an intrinsic response of the coherent eddy  
 381 field. Note that the negative coherent eddy amplitude dominates the global  $|cEddy_{amp}|$   
 382 trends (Figure 9e, f). However, different trend pattern can be observed in both positive  
 383 and negative coherent eddy amplitudes in the north Atlantic and north Pacific, where  
 384 the negative coherent eddy amplitude in the Western Boundary Currents appears to de-  
 385 crease and is consistent with Figure 8.

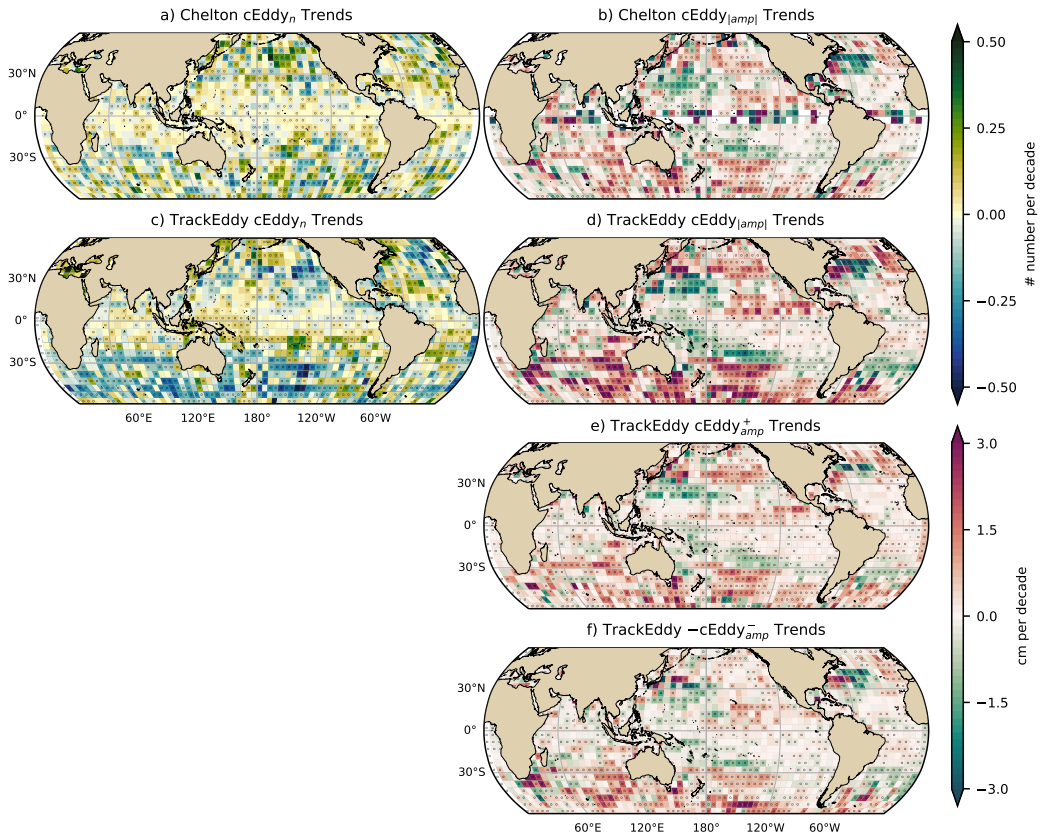
## 393 **6 Regional Climatology**

394 For regions with relatively large proportions of CEKE located at boundary **currents**  
 395 **extensions** and eastern currents, we investigate the seasonal and long-term variability  
 396 of the coherent eddy properties.

397 The most energetic western boundary **currents\_extensions** include; the Gulf Stream,  
 398 the Kuroshio Current, and the Agulhas Current (Figures 10, 11, and 12). Coherent eddy



349 **Figure 8.** Hemispherical seasonality of the coherent eddy statistics; a,e) seasonal cycle of  
 350 the number of coherent eddies ( $cEddy_n$ ); b,f) seasonal cycle-time-series of the mean coherent  
 351 eddy amplitude ( $cEddy_{amp}$ ); c,g) seasonal cycle-climatology of the warm core coherent eddies  
 352 amplitude (positive  $cEddy_{amp}$ ); d,h) seasonal cycle-climatology of the cold core coherent ed-  
 353 dies amplitude (negative  $cEddy_{amp}$ ). Panels a, b, and c show, and d correspond to the northern  
 354 hemisphere seasonal cycle Northern Hemisphere, while panels e, f, and g, and h correspond to  
 355 the southern hemisphere Southern Hemisphere. Dashed lines correspond to the seasonal cycle of  
 356 the fields and dotted lines show the seasonal cycle of the wind magnitude smoothed over 120 days  
 357 (moving average). The green and magenta stars show the maximum of the seasonal cycle for each  
 358 field and the wind magnitude, respectively. The line colors show the year.



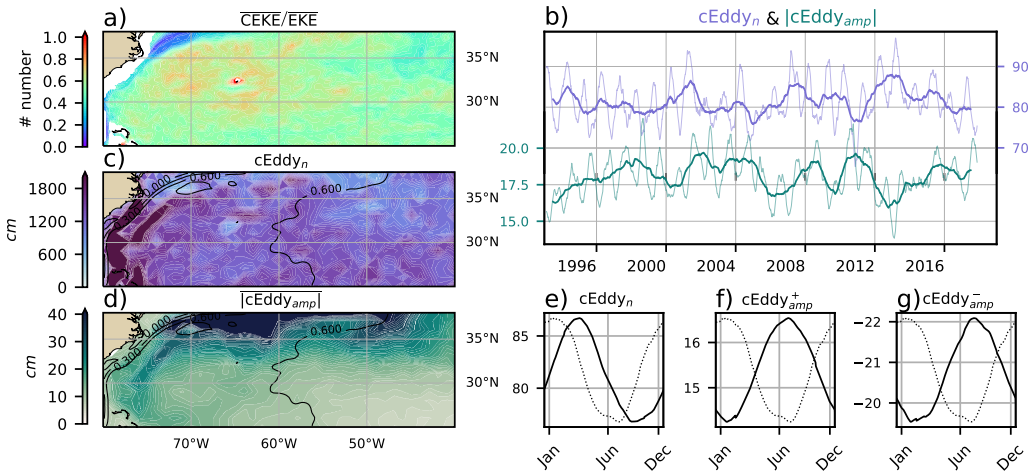
386 **Figure 9.** Trends of coherent eddy statistics. a) and b) Trends of the number of identified  
 387 coherent eddies from satellite observations identified using TrackEddy, and those reported in  
 388 Chelton's dataset. c) and d) Trends of the mean absolute value of identified coherent eddies am-  
 389 plitude from satellite observations identified using TrackEddy, and those reported in Chelton's  
 390 dataset. e) and f) Trends of eddy amplitude polarity using TrackEddy. Gray stippling shows  
 391 regions that are statistically significant above the 95% confidence level. **Change cEddy<sub>|amp|</sub> to**  
 392 **|cEddy<sub>a</sub>mp|**

399 generation in boundary ~~currents~~extensions occurs through baroclinic and barotropic in-  
 400 stabilities of the mean current, thus all these ~~currents~~regions share similar generation  
 401 dynamics. In all these ~~currents~~regions without exception; (i) CEKE contains ~~around up~~  
 402 to 80% of the EKE in regions equatorwards from the mean western boundary ~~current~~  
 403 extension location, (ii) the number of eddies is consistently ~~larger equatorwards from minimal~~  
 404 numbers of eddies over the mean western boundary ~~current~~extension location, and (iii)  
 405 the absolute eddy amplitude is larger polewards of the mean western boundary ~~current~~  
 406 extension location.

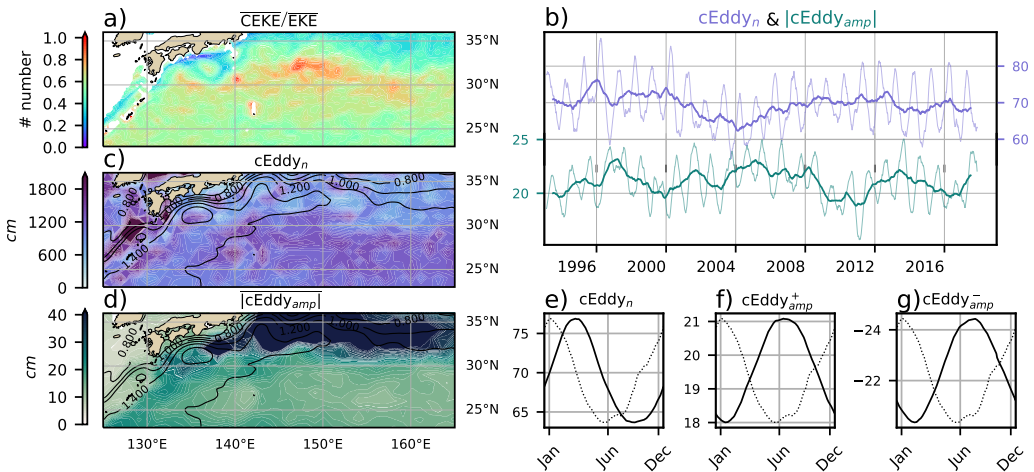
407 In the Gulf Stream, the energy ratio between CEKE and EKE is  $\sim$ 55% (Figure 10).  
 408 The highest energy content occurs in regions with numerous eddies, ~~but is follows closer~~  
 409 by and collocated with regions where the largest  $|cEddy_{amp}|$  gradients occurs. The time  
 410 series of  $cEddy_n$  and  $|cEddy_{amp}|$  are anti-correlated (-0.52), and they display inter-annual  
 411 and seasonal variability. Although Chaudhuri et al. (2009) observed a positive phase of  
 412 North Atlantic Oscillation (NAO) exhibit higher EKE, due to an increase in baroclinic  
 413 instabilities, thus suggesting more coherent eddies, we do not find a correlation between  
 414 the  $cEddy_n$  or the  $|cEddy_{amp}|$  in the Gulf Stream and the NAO index. Similar to the  
 415 signal observed in the hemispherical analysis, the eddy count seasonal cycle follows the  
 416 wind maximum after  $\sim$ 3 months, while the amplitude of the coherent eddies lags by  $\sim$   
 417 6 months.

426 The variability of the  $cEddy_n$  and  $|cEddy_{amp}|$  in the Kuroshio Current are weakly  
 427 anti-correlated (-0.4; Figure 11). However, on average 56% of the energy in the region  
 428 corresponds to CEKE. As observed in the Gulf Stream, there is an important seasonal  
 429 cycle in the boundary ~~current~~extensions, where the eddy count seasonal cycle occurs  
 430 on March after  $\sim$ 3 months of the wind maximum (January). Meanwhile, the amplitude  
 431 of the coherent eddies lags by  $\sim$  6 months (June) after the maximum wind.

438 In the Southern ~~Ocean~~Hemisphere, the strongest boundary current, the Agulhas  
 439 Current ~~show similar behavior than~~shows similar behavior to its counterparts in the North-  
 440 ern ~~hemisphere~~Hemisphere (Figure 12). On average, coherent eddies in the Agulhas cur-  
 441 rent contain  $\sim$ 56% of the energy, meanwhile the  $cEddy_n$  seasonal peak occurs in August,  
 442 while the  $|cEddy_{amp}|$  occurs in January-February. The seasonal lag between the winds,  
 443 eddy count, ~~eddy amplitude, and winds in western boundary currents and eddy amplitude~~  
 444 in each of the western boundary current extensions is interpreted as being analogous to



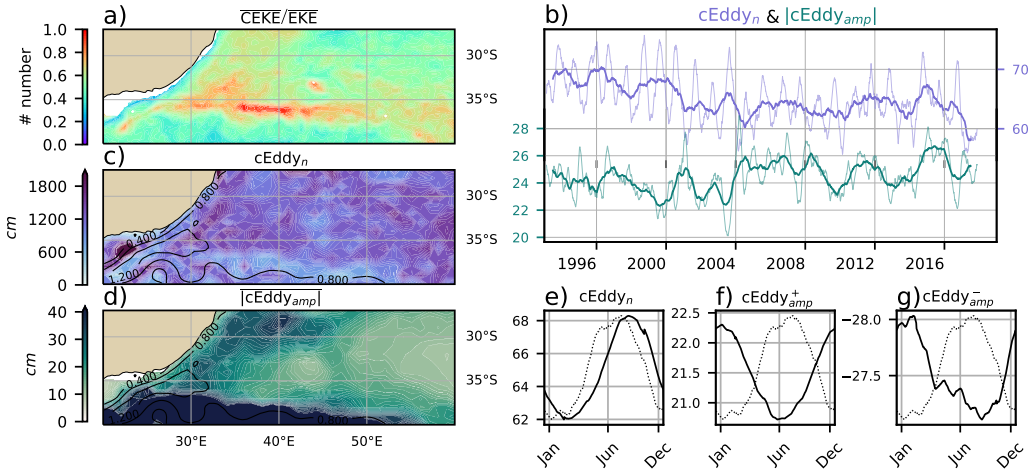
418 **Figure 10.** Climatology of the eddy field and coherent eddy field at the Gulf Stream. a) Ratio  
 419 of mean coherent eddy kinetic energy ( $\overline{\text{CEKE}}$ ) versus mean eddy kinetic energy ( $\overline{\text{EKE}}$ ); b) Thick  
 420 lines show the running average over 2 years and thin lines show the running average over 90 days  
 421 of the coherent eddy number sum and the average absolute coherent eddy amplitude; c) Map of  
 422 the number of eddies; d) Map of the average absolute coherent eddy amplitude; e) Seasonal cycle  
 423 of the number of eddies f) Seasonal cycle of the positive coherent eddy amplitude. g) Seasonal  
 424 cycle of the negative coherent eddy amplitude. Contours in maps correspond to mean sea surface  
 425 height (m).



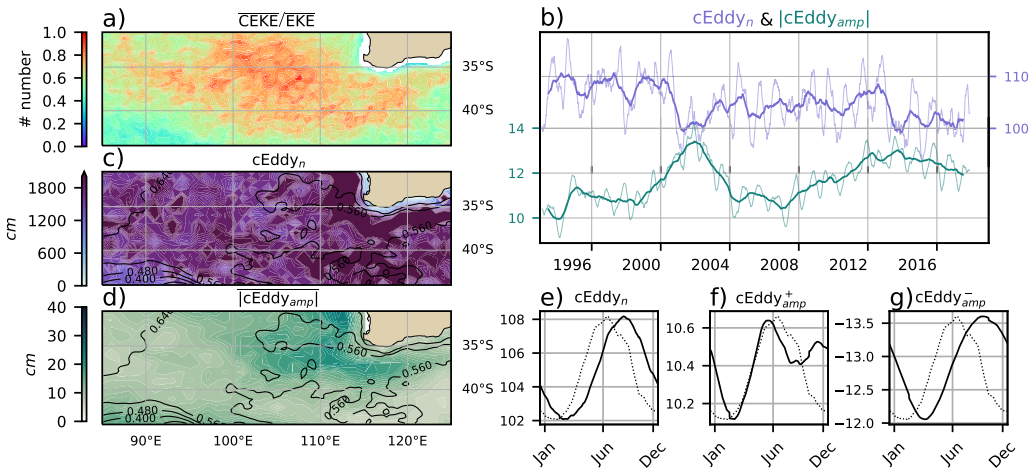
432 **Figure 11.** Climatology of the eddy field and coherent eddy field at the Kuroshio  
 433 **Currentextension.** a) Ratio of mean coherent eddy kinetic energy ( $\overline{CEKE}$ ) versus mean eddy  
 434 kinetic energy ( $\overline{EKE}$ ); b) Time-series of the coherent eddy number and the average absolute co-  
 435 herent eddy amplitude; c) Map of the number of eddies; d) Map of the average absolute coherent  
 436 eddy amplitude; Seasonal cycle of the e) number of eddies, f) positive coherent eddy amplitude,  
 437 and g) negative coherent eddy amplitude. Different lines represent the same as in Figure 10.

445 the explanation ~~presented in section ?? observed in Figure 6~~ of the lagged response of  
 446 coherent eddy properties due to eddy-eddy interactions ~~and, consistent with~~ the inverse  
 447 cascade of energy.

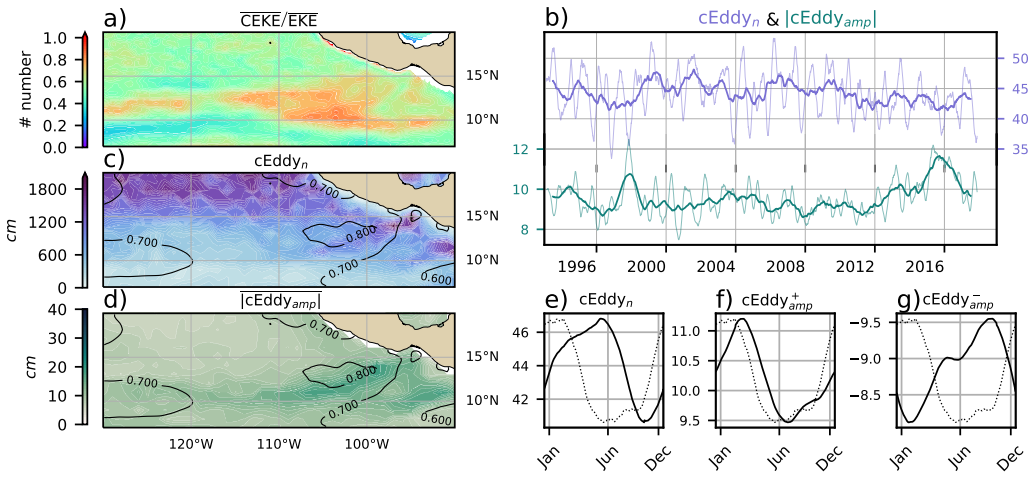
454 ~~Note that coherent Coherent~~ eddies dominate the EKE field in other regions such  
 455 as the Leeuwin Current (Figure 13), where the 65% of the energy is contained by coher-  
 456 ent eddies. Although the Leeuwin region is not characterized by having a large EKE, ~~a~~  
 457 ~~considerable amount of eddies is observable across the region, but more importantly the~~  
 458 ~~coherent eddy amplitude is particularly large in those regions where coherent edddies~~  
 459 ~~dominate~~ however, a considerable abundance of eddies and large eddy amplitudes are observable  
 460 ~~in the region~~. The series reveal a significant increase in the  $|cEddy_{amp}|$ , while the  $cEddy_n$   
 461 has decreased over the last 3 decades ~~Q~~. The seasonal cycle shows that the  $cEddy_n$  peak  
 462 occurs on August, 3 months after the maximum winds (June). Meanwhile, the  $cEddy_{amp}^+$   
 463 responds in synchrony to winds, and the  $cEddy_{amp}^-$  is in phase with the seasonal cycle  
 464 of the  $cEddy_n$ .



448 **Figure 12.** Climatology of the eddy field and coherent eddy field at the Agulhas Current. a)  
449 Ratio of mean coherent eddy kinetic energy ( $\overline{\text{CEKE}}$ ) versus mean eddy kinetic energy ( $\overline{\text{EKE}}$ ); b)  
450 Time-series of the coherent eddy number and the average absolute coherent eddy amplitude; c)  
451 Map of the number of eddies; d) Map of the average absolute coherent eddy amplitude; Seasonal  
452 cycle of the e) number of eddies, f) positive coherent eddy amplitude, and g) negative coherent  
453 eddy amplitude. Different lines represent the same as in Figure 10.



465 **Figure 13.** Climatology of the eddy field and coherent eddy field at the Leeuwin Current. a)  
466 Ratio of mean coherent eddy kinetic energy ( $\overline{\text{CEKE}}$ ) versus mean eddy kinetic energy ( $\overline{\text{EKE}}$ ); b)  
467 Time-series of the coherent eddy number and the average absolute coherent eddy amplitude; c)  
468 Map of the number of eddies; d) Map of the average absolute coherent eddy amplitude; Seasonal  
469 cycle of the e) number of eddies, f) positive coherent eddy amplitude, and g) negative coherent  
470 eddy amplitude. Different lines represent the same as in Figure 10.



484 **Figure 14.** Climatology of the eddy field and coherent eddy field at the East Tropical Pacific.  
485 a) Ratio of mean coherent eddy kinetic energy ( $\overline{CEKE}$ ) versus mean eddy kinetic energy ( $\overline{EKE}$ );  
486 b) Time-series of the coherent eddy number and the average absolute coherent eddy amplitude;  
487 c) Map of the number of eddies; d) Map of the average absolute coherent eddy amplitude; Sea-  
488 sonal cycle of the e) number of eddies, f) positive coherent eddy amplitude, and g) negative  
489 coherent eddy amplitude. Different lines represent the same as in Figure 10.

471 Another region with important contributions of the coherent eddy field is the East  
472 Tropical Pacific (Tehuantepec region; Figure 14), where coherent eddies contain  $\sim 58\%$   
473 of the energy. In fact, coherent eddy generation in this region is modulated by winds and  
474 ~~east coastally~~ trapped waves which produce a strong horizontal and vertical shear (baro-  
475 clinic and barotropic instabilities; Zamudio et al., 2006). Furthermore, the equatorial gen-  
476 erated waves propagating along the coast have an important interannual variability ob-  
477 servable in the  $|cEddy_{amp}|$  time-series, where El Niño events are notable during 1997 and  
478 2015 (Figure 14b). The seasonal cycle of  $cEddy_n$ ,  $cEddy_{amp}^+$ , and  $cEddy_{amp}^-$  ~~supports~~  
479 ~~support~~ the idea of a coherent eddies responding to two different coherent eddy gener-  
480 ation mechanisms; the number of eddies seasonal cycle lags for by  $\sim 3$  months from the  
481 winds, while the  $cEddy_{amp}^+$  is on phase with the winds and the maximum of trapped waves  
482 (winter; Zamudio et al., 2006), and the  $cEddy_{amp}^-$  could be a consequence of eddy-eddy  
483 interactions.

490      **7 Summary-Discussion and Conclusions**

491      We investigated the contribution of coherent ~~eddy~~eddies in the kinetic energy field  
 492      using satellite observations. We corroborate that around half of the EKE is explained  
 493      by coherent eddies. This half is concentrated in eddy-rich regions where an intensification  
 494      of the eddy field has been observed (Martínez-Moreno et al., 2021).

495      The energy contained by eddies is larger than the previous estimate of 40% [by Chelton et al. \(2011\)](#).  
 496      Although there are difference in the identification criteria of both eddy identification  
 497      methods, the main cause of the difference is believed to be the lifespan and amplitude  
 498      filters. ~~Although these~~These filters are widely used to track individual eddies on space  
 499      and time, [however](#), interactions between eddies in energetic regions my obscure ~~their~~the  
 500      abundance and influence of short-lived coherent eddies. Filters are not used in this study,  
 501      and indeed a lack of filters [could](#) facilitates an under or over-estimation of the the en-  
 502      ergy contained by coherent eddies, when miss-identifying or miss-fitting a coherent eddy.  
 503      Thus, the presented estimate represents an upper limit of the energy contained by co-  
 504      herent eddies.

505      In addition, it should be noted that regions with first baroclinic Rossby radius of  
 506      deformation smaller than 10km cannot be resolved by satellite observations. Thus, the  
 507      energy contained by coherent eddies around latitudes of 60° and those near the shore  
 508      are missed from this estimate, and remains unknown their role in the seasonal cycle and  
 509      local dynamics. New satellite altimeter missions (SWOT) may allow to estimate energy  
 510      contained by mesoscale coherent eddies outside the tropical region and the continental  
 511      slope.

512      Hemispherical variability indicates a strong seasonal cycle of the EKE, CEKE, and  
 513      eddy properties. The seasonal cycle of the CEKE in each hemisphere occurs as a con-  
 514      sequence of numerous small coherent eddies interacting with each other (eddy-eddy in-  
 515      teractions) and resulting in stronger, larger and more energetic coherent eddies during  
 516      summer after a few months of the yearly coherent eddy number maxima. This results  
 517      reveals eddy-eddy interactions and thus the transfer of energy from smaller coherent ed-  
 518      dies to larger coherent eddies could explain the observed seasonal cycle of CEKE and  
 519      coherent eddies properties.

520        **Check-values** Coherent eddy properties showcase a non-uniform long-term read-  
 521        justment of the mesoscale eddy field. Overall, the eddy number has decreased globally  
 522        at a negligible-significant rate of  $\sim 35$  eddies per decade from  $\sim 4000$  eddies identified glob-  
 523        ally on average each day. However, large proportions of the ocean show an strengthen-  
 524        ing of the mesoscale coherent eddy field at a rate of greater than  $\sim 5.8-1$  cm per decade.  
 525        **Positive trends average 1cm per decade, negative trends average -0.7cm per**  
 526        **decade. Global average 0.2cm per decade** This strengthening of the coherent eddy  
 527        amplitude is attributed to an intensification of each coherent eddy polarity, rather than  
 528        a readjustment of the coherent eddy field to sea level rise. In other words, the coherent  
 529        eddy amplitude intensification is occurring in both coherent eddy polarities and explain  
 530        a proportion of the previously observed readjustments in the eddy field to long-term changes  
 531        in the ocean forcing (Hu et al., 2020; Wunsch, 2020; Martínez-Moreno et al., 2021). Although,  
 532        the hypothesis of more eddy-eddy interactions and thus This long-term readjustment showcases  
 533        an intensification of the inverse energy cascade can be extended to explain the long-term  
 534        readjustment of the coherent eddy field, this possibly due to long-term readjustment could  
 535        incorporate additional long-term readjustments such as: changes in readjustments in the  
 536        ocean baroclinic and barotropic instabilities, stratification and as well as the strength  
 537        of the winds.

538        The reconstruction of the coherent eddies and their statistics have revealed regions  
 539        with important coherent eddy contributions and a distinct seasonal evolution of the co-  
 540        herent eddies. Remarkably, western boundary currents-extensions generate eddies through  
 541        the instability of the main currents and the seasonal cycle of coherent eddies, CEKE, and  
 542        thus EKE could be associated with an inverse energy cascade observable through lagged  
 543        seasonal cycles in the coherent eddy statistics. In addition to this, the amplitude of the  
 544        seasonal cycle in the boundary currents-extensions is two times larger than any other  
 545        region, thus the seasonality of the coherent eddies in boundary currents-extensions dom-  
 546        inate the hemispherical seasonal cycle. Furthermore, the seasonal lag of the inverse en-  
 547        ergy cascade is coupled with the presence of fronts, such is the case of western bound-  
 548        ary currents-extensions, and our results are consistent with the notion of baroclinic in-  
 549        stability generating eddies and through eddy-eddy interactions an lagged inverse energy  
 550        cascade.

551        The use of satellite observations in this study limit our ability to quantify the im-  
 552        portance of the inverse energy cascade seasonality in the control of the coherent eddy

553 seasonal cycle. As mentioned above, there is robust evidence of an increase in eddy-eddy  
 554 interactions, however we can not discard important contributions from other processes  
 555 such as the seasonal cycle of forcing and instabilities, which are crucial in the genera-  
 556 tion of coherent eddies. Although this study can provide a descriptive response of the  
 557 coherent eddy field, further studies are needed to asses the role of eddy-eddy interactions  
 558 in our changing climate, ocean dynamics, and biogeochemical process. Furthermore, the  
 559 SWOT mission ~~would~~could allow to advance our understanding of eddy-eddy interac-  
 560 tions and the seasonal cycle of scales smaller than mesoscale, which may provide further  
 561 evidence of the inverse energy cascade driving the coherent eddy seasonality.

## 562 Acknowledgments

563 Chelton & Schlax (2013) dataset was produced by SSALTO/DUACS and distributed by  
 564 AVISO+ (<https://www.aviso.altimetry.fr/>) with support from CNES, developed  
 565 and validated in collaboration with E.Mason at IMEDEA. Global coherent eddy recon-  
 566 struction, coherent and non-conherent eddy kinetic energy datasets, in addition to grid-  
 567 ded coherent eddy tracking datasets are publicly available at (<https://doi.org/10.5281/zenodo.4646429>). All analyses and figures in this manuscript are reproducible via Jupyter  
 568 notebooks and instructions can be found in the Github repository `CEKE_climatology`  
 569 ([https://github.com/josuemtzmo/CEKE\\_climatology](https://github.com/josuemtzmo/CEKE_climatology)). Trends used the Python Pack-  
 570 age `xarrayMannKendall` (<https://doi.org/10.5281/zenodo.4458776>)

## 572 References

- 573 Arbic, B. K., Polzin, K. L., Scott, R. B., Richman, J. G., & Shriver, J. F. (2013).  
 574 On Eddy Viscosity, Energy Cascades, and the Horizontal Resolution of Gridded  
 575 Satellite Altimeter Products\*. *Journal of Physical Oceanography*, 43(2), 283–300.  
 576 doi: 10.1175/jpo-d-11-0240.1
- 577 Ashkezari, M. D., Hill, C. N., Follett, C. N., Forget, G., & Follows, M. J. (2016).  
 578 Oceanic eddy detection and lifetime forecast using machine learning methods.  
 579 *Geophysical Research Letters*, 43(23). doi: 10.1002/2016gl071269
- 580 Beron-Vera, F. J., Wang, Y., Olascoaga, M. J., Goni, G. J., & Haller, G. (2013). Ob-  
 581 jective Detection of Oceanic Eddies and the Agulhas Leakage. *Journal of Physical  
 582 Oceanography*, 43(7), 1426–1438. doi: 10.1175/JPO-D-12-0171.1
- 583 Bouali, M., Sato, O. T., & Polito, P. S. (2017). Temporal trends in sea surface tem-

- 584      perature gradients in the South Atlantic Ocean. *Remote Sensing of Environment*,  
 585      194, 100–114. doi: 10.1016/j.rse.2017.03.008
- 586      Callies, J., Flierl, G., Ferrari, R., & Fox-Kemper, B. (2015). The role of mixed-layer  
 587      instabilities in submesoscale turbulence. *Journal of Fluid Mechanics*, 788, 5–41.  
 588      doi: 10.1017/jfm.2015.700
- 589      Cane, M. A., Clement, A. C., Kaplan, A., Kushnir, Y., Pozdnyakov, D., Seager, R.,  
 590      ... Murtugudde, R. (1997). Twentieth-Century Sea Surface Temperature Trends.  
 591      *Science*, 275(5302), 957–960. doi: 10.1126/science.275.5302.957
- 592      Chaudhuri, A. H., Gangopadhyay, A., & Bisagni, J. J. (2009). Interannual variabil-  
 593      ity of Gulf Stream warm-core rings in response to the North Atlantic Oscillation.  
 594      *Continental Shelf Research*, 29(7), 856–869. doi: 10.1016/j.csr.2009.01.008
- 595      Chelton, D. B., A. d. R., Schlax, M. G., Naggar, K., & Siwetz, N. (1998). Geo-  
 596      graphical variability of the first baroclinic Rossby radius of deformation. *Journal*  
 597      *of Physical Oceanography*, 28(3), 433–460. doi: 10.1175/1520-0485(1998)028<433:  
 598      GVOTFB>2.0.CO;2
- 599      Chelton, D. B., Gaube, P., Schlax, M. G., Early, J. J., & Samelson, R. M. (2011).  
 600      The influence of nonlinear mesoscale eddies on near-surface oceanic chlorophyll.  
 601      *Science*, 334(6054), 328–32. doi: 10.1126/science.1208897
- 602      Chelton, D. B., & Schlax, M. G. (2013). *Mesoscale eddies in altimeter observations*  
 603      *of ssh*.
- 604      Chelton, D. B., Schlax, M. G., Samelson, R. M., & de Szoeke, R. A. (2007). Global  
 605      observations of large oceanic eddies. *Geophysical Research Letters*, 34(15),  
 606      L15606. doi: 10.1029/2007GL030812
- 607      CMEMS. (2017). The Ssalto/Duacs altimeter products were produced and dis-  
 608      tributed by the Copernicus Marine and Environment Monitoring Service. *Aviso*  
 609      *Dataset*. Retrieved from <https://www.aviso.altimetry.fr/>
- 610      Cui, W., Wang, W., Zhang, J., & Yang, J. (2020). Identification and census statis-  
 611      tics of multicore eddies based on sea surface height data in global oceans. *Acta*  
 612      *Oceanologica Sinica*, 39(1), 41–51. doi: 10.1007/s13131-019-1519-y
- 613      Faghmous, J. H., Frenger, I., Yao, Y., Warmka, R., Lindell, A., & Kumar, V. (2015,  
 614      6). A daily global mesoscale ocean eddy dataset from satellite altimetry. *Scientific*  
 615      *Data*, 2, 150028 EP -. doi: 10.1038/sdata.2015.28
- 616      Ferrari, R., & Wunsch, C. (2009). Ocean Circulation Kinetic Energy: Reservoirs,

- 617 Sources, and Sinks. *Annual Review of Fluid Mechanics*, 41(1), 253–282. doi: 10  
618 .1146/annurev.fluid.40.111406.102139
- 619 Frenger, I., Gruber, N., Knutti, R., & Münnich, M. (2013). Imprint of Southern  
620 Ocean eddies on winds, clouds and rainfall. *Nature Geoscience*, 6(8), 608 EP -.  
621 doi: 10.1038/ngeo1863
- 622 Frenger, I., Münnich, M., Gruber, N., & Knutti, R. (2015). Southern Ocean eddy  
623 phenomenology. *Journal of Geophysical Research: Oceans*, 120(11), 7413-7449.  
624 doi: 10.1002/2015JC011047
- 625 Fu, L., Chelton, D., Le Traon, P., & Oceanography, M. R. (2010). Eddy dynamics  
626 from satellite altimetry. *Oceanography*, 23(4), 14-25. doi: 10.2307/24860859
- 627 Gill, A., Green, J., & Simmons, A. (1974). Energy partition in the large-scale ocean  
628 circulation and the production of mid-ocean eddies. *Deep Sea Res Oceanogr Abstr*,  
629 21(7), 499-528. doi: 10.1016/0011-7471(74)90010-2
- 630 Hogg, A. M., & Blundell, J. R. (2006). Interdecadal variability of the southern  
631 ocean. *Journal of Physical Oceanography*, 36(8), 1626-1645. doi: 10.1175/  
632 JPO2934.1
- 633 Hogg, A. M., Meredith, M. P., Chambers, D. P., Abrahamsen, E. P., Hughes,  
634 C. W., & Morrison, A. K. (2015). Recent trends in the Southern Ocean  
635 eddy field. *Journal of Geophysical Research: Oceans*, 120(1), 257-267. doi:  
636 10.1002/2014JC010470
- 637 Hu, S., Sprintall, J., Guan, C., McPhaden, M. J., Wang, F., Hu, D., & Cai,  
638 W. (2020, 2). Deep-reaching acceleration of global mean ocean circula-  
639 tion over the past two decades. *Science Advances*, 6(6), eaax7727. doi:  
640 10.1126/sciadv.aax7727
- 641 Japan Meteorological Agency, Japan. (2013). *Jra-55: Japanese 55-year reanalysis,*  
642 *daily 3-hourly and 6-hourly data.* Boulder CO: Research Data Archive at the Na-  
643 tional Center for Atmospheric Research, Computational and Information Systems  
644 Laboratory. Retrieved from <https://doi.org/10.5065/D6HH6H41>
- 645 Kang, D., & Curchitser, E. N. (2013). Gulf stream eddy characteristics in a high-  
646 resolution ocean model. *Journal of Geophysical Research: Oceans*, 118(9), 4474-  
647 4487. Retrieved from <https://agupubs.onlinelibrary.wiley.com/doi/abs/10.1002/jgrc.20318> doi: <https://doi.org/10.1002/jgrc.20318>
- 648 Kang, D., & Curchitser, E. N. (2017). On the Evaluation of Seasonal Variability of

- 650 the Ocean Kinetic Energy. *Geophysical Research Letters*, 47, 1675–1583. doi: 10  
651 .1175/JPO-D-17-0063.1
- 652 Li, G., Cheng, L., Zhu, J., Trenberth, K. E., Mann, M. E., & Abraham, J. P. (2020).  
653 Increasing ocean stratification over the past half-century. *Nature Climate Change*,  
654 1–8. doi: 10.1038/s41558-020-00918-2
- 655 Martínez-Moreno, J., Hogg, A. M., England, M., Constantinou, N. C., Kiss, A. E.,  
656 & Morrison, A. K. (2021). Global changes in oceanic mesoscale currents over the  
657 satellite altimetry record. *Journal of Advances in Modeling Earth Systems*, 0(ja).  
658 doi: 10.1029/2019MS001769
- 659 Martínez-Moreno, J., Hogg, A. M., Kiss, A. E., Constantinou, N. C., & Morrison,  
660 A. K. (2019). Kinetic energy of eddy-like features from sea surface altimeter-  
661 try. *Journal of Advances in Modeling Earth Systems*, 11(10), 3090–3105. doi:  
662 10.1029/2019MS001769
- 663 Patel, R. S., Llort, J., Strutton, P. G., Phillips, H. E., Moreau, S., Pardo, P. C.,  
664 & Lenton, A. (2020). The Biogeochemical Structure of Southern Ocean  
665 Mesoscale Eddies. *Journal of Geophysical Research: Oceans*, 125(8). doi:  
666 10.1029/2020jc016115
- 667 Pilo, G. S., Mata, M. M., & Azevedo, J. L. L. (2015). Eddy surface properties and  
668 propagation at Southern Hemisphere western boundary current systems. *Ocean  
669 Science*, 11(4), 629–641. doi: 10.5194/os-11-629-2015
- 670 Qiu, B. (1999). Seasonal Eddy Field Modulation of the North Pacific Subtropical  
671 Countercurrent: TOPEX/Poseidon Observations and Theory. *Journal of Physical  
672 Oceanography*, 29(10), 2471–2486. doi: 10.1175/1520-0485(1999)029<2471:sefmot>2  
673 .0.co;2
- 674 Qiu, B., & Chen, S. (2004). Seasonal Modulations in the Eddy Field of the South  
675 Pacific Ocean. *Journal of Physical Oceanography*, 34(7), 1515–1527. doi: 10.1175/  
676 1520-0485(2004)034<1515:smitef>2.0.co;2
- 677 Qiu, B., Chen, S., Klein, P., Sasaki, H., & Sasai, Y. (2014). Seasonal Mesoscale  
678 and Submesoscale Eddy Variability along the North Pacific Subtropical Coun-  
679 tercurrent. *Journal of Physical Oceanography*, 44(12), 3079–3098. doi:  
680 10.1175/JPO-D-14-0071.1
- 681 Ruela, R., Sousa, M. C., deCastro, M., & Dias, J. M. (2020). Global and regional  
682 evolution of sea surface temperature under climate change. *Global and Planetary*

- 683        *Change*, 190, 103190. doi: 10.1016/j.gloplacha.2020.103190
- 684        Sasaki, H., Klein, P., Qiu, B., & Sasai, Y. (2014). Impact of oceanic-scale inter-  
685        actions on the seasonal modulation of ocean dynamics by the atmosphere. *Nature  
686        Communications*, 5(1), 5636. doi: 10.1038/ncomms6636
- 687        Schubert, R., Schwarzkopf, F. U., Baschek, B., & Biastoch, A. (2019). Submesoscale  
688        Impacts on Mesoscale Agulhas Dynamics. *Journal of Advances in Modeling Earth  
689        Systems*, 11(8), 2745–2767. doi: 10.1029/2019ms001724
- 690        Siegel, D., Peterson, P., DJ, M., Maritorena, S., & Nelson, N. (2011). Bio-optical  
691        footprints created by mesoscale eddies in the Sargasso Sea. *Geophysical Research  
692        Letters*, 38(13), n/a-n/a. doi: 10.1029/2011GL047660
- 693        Uchida, T., Abernathey, R., & Smith, S. (2017). Seasonality of eddy kinetic energy  
694        in an eddy permitting global climate model. *Ocean Modelling*, 118, 41-58. doi: 10  
695        .1016/j.ocemod.2017.08.006
- 696        Wunsch, C. (2020). Is The Ocean Speeding Up? Ocean Surface Energy Trends.  
697        *Journal of Physical Oceanography*, 50(11), 1–45. doi: 10.1175/jpo-d-20-0082.1
- 698        Wunsch, C., & Ferrari, R. (2004). Vertical mixing, energy, and the general circula-  
699        tion of the oceans. *Annual Review of Fluid Mechanics*, 36(1), 281–314. doi: 10  
700        .1146/annurev.fluid.36.050802.122121
- 701        Wyrtki, K., Magaard, L., & Hager, J. (1976). Eddy energy in the oceans. *Journal of  
702        Geophysical Research*, 81(15), 2641-2646. doi: 10.1029/JC081i015p02641
- 703        Yue, S., & Wang, C. (2004). The Mann-Kendall Test Modified by Effective Sample  
704        Size to Detect Trend in Serially Correlated Hydrological Series. *Water Resources  
705        Management*, 18(3), 201–218. doi: 10.1023/b:warm.0000043140.61082.60
- 706        Zamudio, L., Hurlburt, H. E., Metzger, E. J., Morey, S. L., O'Brien, J. J., Tilburg,  
707        C., & Zavala-Hidalgo, J. (2006). Interannual variability of Tehuantepec ed-  
708        dies. *Journal of Geophysical Research: Oceans (1978–2012)*, 111(C5). doi:  
709        10.1029/2005JC003182